Ultrafast nanometric imaging of energy flow within and between single carbon dots

Huy A. Nguyen[a,b], Indrajit Srivastava[c,d], Dipanjan Pan[e,f,g], and Martin Gruebele[a,b,h,1]

[a]Department of Chemistry, University of Illinois at Urbana–Champaign, Urbana, IL 61801; [b]Beckman Institute for Advanced Science and Technology, University of Illinois at Urbana–Champaign, Urbana, IL 61801; [c]Department of Bioengineering, University of Illinois at Urbana–Champaign, Urbana, IL 61801; [d]Department of Electrical and Computer Engineering, University of Illinois at Urbana–Champaign, Urbana, IL 61801; [e]Department of Chemical, Biochemical and Environmental Engineering, University of Maryland, Baltimore County, Baltimore, MD 21250; [f]Department of Diagnostic Radiology and Nuclear Medicine, Center for Blood Oxygen Transport & Hemostasis (CBOTH), University of Maryland, Baltimore, MD 21201; [g]Department of Pediatrics, University of Maryland, Baltimore, MD 21201; and [h]Department of Physics, University of Illinois at Urbana–Champaign, Urbana, IL 61801

Edited by Robert W. Field, Massachusetts Institute of Technology, Cambridge, MA, and approved February 2, 2021 (received for review November 4, 2020)

Time- and space-resolved excited states at the individual nanoparticle level provide fundamental insights into heterogeneous energy, electron, and heat flow dynamics. Here, we optically excite carbon dots to image electron–phonon dynamics within single dots and nanoscale thermal transport between two dots. We use a scanning tunneling microscope tip as a detector of the optically excited state, via optical blocking of electron tunneling, to record movies of carrier dynamics in the 0.1–500-ps time range. The excited-state electron density migrates from the bulk to molecular-scale (∼1 nm^2) surface defects, followed by heterogeneous relaxation of individual dots to either long-lived fluorescent states or back to the ground state. We also image the coupling of optical phonons in individual carbon dots with conduction electrons in gold as an ultrafast energy transfer mechanism between two nearby dots. Although individual dots are highly heterogeneous, their averaged dynamics is consistent with previous bulk optical spectroscopy and nanoscale heat transfer studies, revealing the different mechanisms that contribute to the bulk average.

femtosecond imaging | SMA-STM | transient absorption | single-particle dynamics | carbon dots

The use of nanomaterials in a wide variety of applications can be hampered or enhanced by the presence of defects (1), which can change the properties of particles from one to the next. For example, catalysis often occurs at defect sites (2, 3), but only a minority of such sites are catalytic (4); likewise, energy transfer from a quantum dot film to another layer can be focused on specific defect sites rather than being uniform throughout the layer (5).

Excited-state defects in particular control electron, phonon, and energy flow that is important for chemistry and photophysics at the surface of nanomaterials. For some types of nanoparticles, localized surface excited states, rather than particle size, control multicolor emission dynamics (6, 7). Progress has been made in the imaging and tomography of individual excited-state defects with subnanometer resolution in a range of materials (8–10). These techniques probe spatial resolution in exquisite detail, but they lack the time resolution required for revealing the excited-state dynamics directly.

Here we present time-resolved single-molecule absorption scanning tunneling microscopy (trSMA-STM), which uses an STM tip as a photodetector of pump–probe laser excitation, making the spatial resolution independent of wavelength and the time resolution controlled by the laser pulse width. We use trSMA-STM to image the dynamics of single carbon dots and pairs of carbon dots with 100-fs time- and single-nanometer spatial resolution. Carbon dots are a new class of photoluminescent nanomaterials similar in size to quantum dots (<10 nm in diameter) synthesized via hydro-/solvothermal reactions, laser ablation, or microwave treatments. They contain largely sp^2-hybridized carbon oxidized by oxygen- and nitrogen-containing defects. Carbon dots have emerged in bioimaging and energy-related applications, owing to their aqueous solubility, low toxicity, and biocompatibility (11–13).

We find that excited-state dynamics of carbon dots is highly heterogeneous, with some dots relaxing immediately back to the ground state in a few picoseconds, while in other dots the energy is trapped in highly localized and long-lived surface states. These two classes of dots combine in the bulk to produce the known moderate fluorescence quantum yield of carbon-dot ensembles. We also study colocalized pairs of carbon dots, and for such pairs, we see the transfer of energy in a few square-nanometer regions mediated by plasmonic excitation of the surface, revealing the difference between highly confined and bulk heat conductivity

Results

Detection of Transient Absorption of Single Nanoparticles at Room Temperature. trSMA-STM works by modulating the pump and probe lasers and imaging the excited state via the STM tunneling current modulation at ≤1-nm spatial resolution (14, 15): Excitation by the pump beam places an electron into a previously empty orbital near the tunneling energy and results in partial blockage of tunneling through the optically excited state (8), whereas subsequent excitation by the probe beam empties that spin orbital and again opens up the tunneling path. Fig. 1 shows the schematic of the time-resolved instrument, trSMA–STM. It comprises an optical Mach–Zehnder interferometer to provide femtosecond time resolution, and the STM tip to provide single-nanometer spatial resolution, which is therefore independent of laser beam size (*SI Appendix*, Figs. S1–S3).

A Ti:sapphire laser is split into two time-delayed pulse trains, one of which is frequency-doubled to blue light (400 nm) for the pump; the other is delayed on a stage and used as the probe (800

Significance

Carbon dots are promising fluorescent nanomaterials, but their fluorescence yield is fairly low when measured in the bulk. By observing single dots directly using femtosecond single-nanometer resolution imaging, we find that some carbon dots fluoresce exceedingly well and others not at all. We propose a simple mechanism, which suggests that near-perfect fluorescence yield is possible by improved separation or synthesis, as indeed quantum yields of carbon dots have been improving.

Author contributions: M.G. designed research; H.A.N. and I.S. performed research; D.P. contributed new reagents/analytic tools; H.A.N., I.S., and M.G. analyzed data; H.A.N. and M.G. wrote the paper; and I.S. and D.P. edited the paper.

The authors declare no competing interest.

This article is a PNAS Direct Submission.

[1]To whom correspondence may be addressed. Email: mgruebel@illinois.edu.

This article contains supporting information online at https://www.pnas.org/lookup/suppl/doi:10.1073/pnas.2023083118/-/DCSupplemental.

Published March 8, 2021.

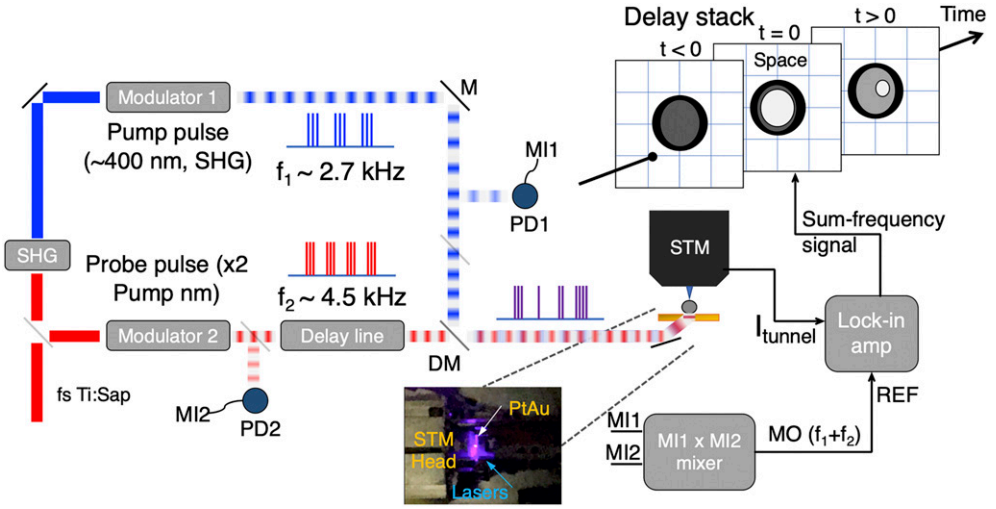

Fig. 1. Schematic of trSMA-STM. A sub-100 fs Ti:sapphire pulse train (*Bottom Left*) is split into two beams: one arm generates the blue second harmonic (SHG) by frequency-doubling the red input pulse; the other arm is time-delayed for transient absorption imaging. The two beams are amplitude-modulated at noncommensurate frequencies f_1 and f_2 and recombined collinearly onto the tip–sample junction (STM). The photograph (*Top View*) shows how the lasers (blue arrow) back-illuminate the PtAu thin film (gold) to reach the carbon dot. The tunneling current from the STM, sensitive to excited-state electrons blocking tunneling, is heterodyne-detected at the sum frequency (2.7+4.5 = 7.2 kHz) of the laser beams by a lock-in amplifier and spatially mapped together with the conventional (average tunneling current) STM image. The delay line allows trSMA-STM images to be collected with successive pump–probe delays to create a stack of time-resolved images (*Top Right*), in which excitation (light) is initially delocalized and becomes localized.

nm). The two beams are modulated at different kHz frequencies such that the sum frequency lies near the mechanical bandwidth but below the electronic bandwidth of the STM scanner. They are recombined and sent collinearly through the rear of the substrate. The sample is excited by the evanescent wave following total internal reflection to avoid tip heating.

Heterodyne demodulation of the tunneling current yields an image proportional to the transient absorption within ~80 s of signal averaging for each picosecond delay time (*SI Appendix*, Fig. S4): the probe pulse depletes the excited state, restoring tunneling through that state (8). Thus, for acquiring an excited-state transient absorption movie with 20 frames, the sample has to remain stable for 1,600 s at ~10-mW laser power in an ~0.1 × 0.1-mm^2 spot. A grayscale map represents the amplitude of the tunneling current modulation due to both beams simultaneously. White indicates maximum excited-state absorption, black minimum. The pump–probe delay stack in Fig. 1 (*Top Right*) shows a cartoon of a carbon dot undergoing excitation at t = 0 and decay to a localized surface defect at t > 0. Each dot was scanned twice (forward and reverse STM trace) to ensure the reproducibility of the signal. As shown previously (7), tip perturbation of the carbon-dot bandgaps at low tunneling current (100 pA) and voltage (~1 V) is small. However, Stark shift perturbations that occur at high field can be imaged for carbon materials (16).

A Simple Model to Guide the Experimental Interpretation and Analysis. The single-dot STM movies of all observed dots will be modeled in *Discussion* by the four-level system in Fig. 2. "g" is the ground state, "c" the delocalized excited core state, "s" a localized excited surface state, and "f" a long-lived relaxed surface state. Composed mainly of sp^2 carbon domains, state c has a high absorption cross-section for the 400-nm pump pulse, which populates the excited core state of the carbon dot. The absorbed energy then migrates from the core to an excited surface state s in τ_{cs} ~400 fs for all dots. From there, the energy can follow one of two different paths: In path 1, rapid relaxation with time constant τ_{sg} returns the dot to the ground state (*SI Appendix*, Figs. S7, S9, and S10). In path 2, state s instead relaxes with time constant τ_{sf} to the long-lived relaxed surface state f. In path 2, the long-lived surface state has a high probability of eventually decaying to the ground state by fluorescence with time constant τ_{fg}. States "s" and "f" could result from excitation of heteroatom defects in the polycyclic carbon network at the surface, or from excitation of molecular moieties integrated into the carbon dot structure (17).

Femtosecond Imaging of Individual Carbon-Dot Dynamics. We studied in detail 12 blue-emitting carbon dots prepared and deposited

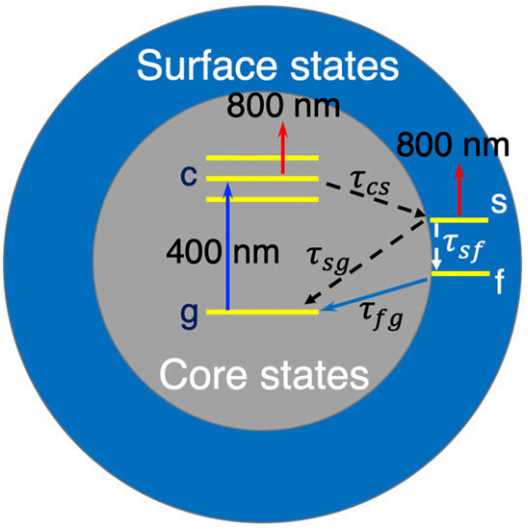

Fig. 2. Kinetic model. The schematic of the four-level kinetic model shows pump (blue vertical arrow) and probe (red vertical arrows) beam absorption as well as labeling states and relaxation times. All relaxation processes were treated as irreversible in this model. In both paths 1 and 2, the dot is excited first (blue vertical arrow) to core state c and relaxes with time constant τ_{cs} to a surface defect s. On path 1, the dot then directly relaxes back to the ground state with time constant τ_{sg} because state s cannot access state f. On path 2, the dot relaxes with time constant τ_{sf} from s to a long-lived relaxed surface state f, from where it can fluoresce back down to the ground state with time constant τ_{fg}. In the experiments (Fig. 3 and *SI Appendix*) 11 out of 12 dots followed only one of the paths, while one dot had comparable lifetimes τ_{sf} and τ_{sg} that could be fitted simultaneously.

on a gold substrate as described in ref. 7. Dots were selected at random by their ≤10-nm diameter, separation of at least 20 nm from other dots, and round appearance to avoid aggregates, as well as optimal imaging conditions that depend on STM tip quality. Fig. 3 shows three examples of carbon-dot trSMA-STM images and transient absorption time series. In accordance with the model, we observe a subpicosecond rise of the signal in all dots as the delocalized core excited state is populated (Fig. 3*A*). At negative time delay $t < 0$ we observe some transient absorption from midgap states identified in ref. 7, which we do not analyze here in detail. The rise at $t > 0$ is followed by heterogeneous picosecond relaxation dynamics either to a long-lived state (Fig. 3*A*, rows 1 and 2) or back to the ground state (Fig. 2*A*, row 3). Each time series in Fig. 3*A* is extracted from the corresponding image stack in Fig. 3*B* by weight-averaging the major time-dependent eigen-assays obtained by singular value decomposition of an image stack. The time series are then smoothed by a three-point box average before fitting to the kinetics model (see *SI Appendix* and *Discussion*).

Individual pump–probe traces (Fig. 3*A* and *SI Appendix*, Figs. S5–S16) fall into two classes: 1) rapid relaxation and 2) long-lived (>500 ps) surface state in a 3:9 ratio. Thus, our average fluorescence quantum yield in the ultrahigh vacuum is likely closer to ∼75% than the ∼20% measured in ethanol solution. The ultrahigh-vacuum condition eliminates the quenching environment due to polar solution (18), a trend we verified for our dots by comparing alcohol (less polar) and alcohol–aqueous mixtures (more polar; see *SI Appendix*, Fig. S17).

The trSMA-STM image of excited-state electron density for dots with long-lived excited states evolves in 2–10 ps from covering the whole core of the dot to an ∼1-nm^2 spot of enhanced tunneling current (Fig. 3*B*): absorbed energy moves to localized defects during the decay in Fig. 3*A*. In a previous SMA-STM study of carbon dots without time resolution (7), we demonstrated that fluorescence originates from a localized region on the surface of the carbon dot. Thus, trSMA-STM directly observes the pathway of migration of excitation from a delocalized core state to a long-lived localized surface state. For some transients, the signal increases at the very end due to energy dissipation into the surface. We explain this phenomenon next.

Dot-To-Dot and Dot-To-Surface Energy Flow. We further explored the process of dot relaxation to observe how such relaxation eventually leads to energy transfer between dots and to the substrate. The system is now a pair of carbon dots separated by up to a few nanometers (Fig. 4). The dots in Fig. 3 straddle nanoscale clefts between gold islands.

The two dots in Fig. 4*A* are in close contact. Their transient absorption signals decay jointly in ∼10 ps (red and blue traces in Fig. 4*B* overlap), while carriers are excited in the cleft between dots earlier than the rest of the gold surface in Fig. 4 *C*, *i–iii* (darkening of the surface).

Fig. 4*D* shows two dots separated by ∼6 nm. In Fig. 4*E*, transient absorption has a rebound and the upper dot (red) lags the lower dot (blue) by ∼25 ps. After 1 ps, excited carriers (darker signal on the gold) appear between the dots and near the lower dot first (Fig. 4 *F*, ii), and finally conform to the shape of the gold valley at the bottom after 100 ps (Fig. 4 *F*, iii).

Therefore, energy flow to the substrate and to other dots already takes place on the longer timescale of intradot dynamics (tens of picoseconds) for those dots that are able to relax rapidly as opposed to remaining in a long-lived excited state waiting to fluoresce. Both the intradot and interdot energy pathways can be understood by kinetic models.

Discussion

A Simple Model for Heterogeneous Excited-State Lifetimes Reconciles Single-Particle and Bulk Data. We implemented the model in Fig. 2 by solving a system of four differential equations numerically. The model quantitatively describes the 12 single-dot traces at $t \geq 0$ (Fig. 3 and *SI Appendix*, Figs. S5–S16) by assuming irreversible steps from core c to surface defect s, and from there either back to the ground state g or a long-lived relaxed surface state f. Fitting the model to the single-particle traces yields the lifetimes and signal ratios of the excited states (Table 1 and *SI Appendix*, Table S1). The lifetimes describe the unique dynamics of each dot, whereas the signal ratios describe the relative contributions of signals from transient absorption in each of the three excited states.

Regarding the lifetimes, our model shows that one of the two energy paths 1 or 2 dominates in most carbon dots, with a single exception, where $\tau_{sg} \sim \tau_{sf}$ and the two paths could be fitted

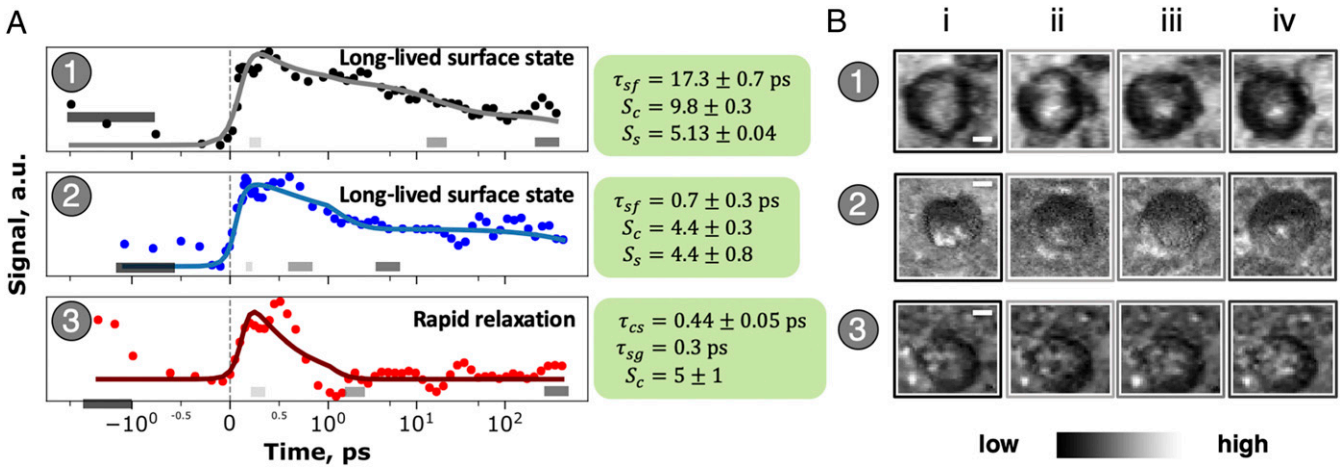

Fig. 3. Space- and time-resolved relaxation dynamics of blue-emitting individual carbon dots. (*A, 1–3*) Transient absorption of carbon dots by trSMA-STM. The gray-colored strip indicates the time span over which the images are averaged. The 0–1-ps range is plotted linearly, 1–500 ps logarithmically. Fits for all 12 individual dots observed are shown in *SI Appendix*. Three dots relaxed rapidly back to the ground state, and nine were trapped in long-lived defects. The signal before $t = 0$ is due to gap-state absorption of the 800-nm light by the dots. (*B, 1–3*) trSMA-STM images of individual dots averaged over the time windows *i* through *iv* indicated by gray-colored strips in *A*; For dots 1 and 2, the excited state evolves from a more delocalized core state toward a localized long-lived defect state. (Scale bars, 2 nm.) STM scanning conditions: 1.3 V, 50 pA; laser power density: 1.3–3 W/mm^2 (pump, 400-nm laser wavelength), 1.5 W/mm^2 (probe, 800-nm laser wavelength).

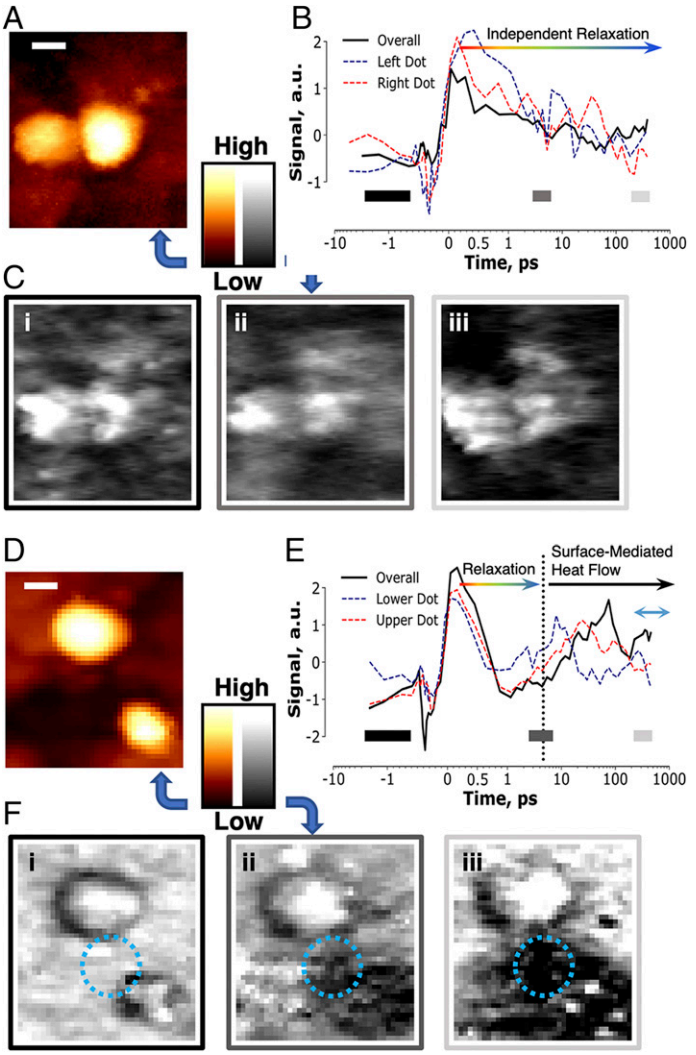

Fig. 4. Observation of independent relaxation and energy transfer by surface-mediated heat flow between blue carbon dots. (*A*) Topographic image of two dots that relax independently. (*B*) Pump–probe traces using the same analysis as Fig. 3 for both dots (solid black line) and each individual dot (dashed lines). Independent relaxation of each dot is indicated by the rainbow arrow. The gray bars indicate the time range for the images in *C*. (*C*, *i–iii*) trSMA-STM images; *ii* and *iii* show evidence of general surface heating from 5 to 200 ps (lower trSMA-STM signal due to excited electrons blocking tunneling equal darker background). STM scanning conditions: 1.3 V, 50 pA. (*D*) Topographic image of two dots that relax and exchange energy via heat flow through the intervening surface. (*E*) Pump–probe traces for both dots (solid black line) and each individual dot (dashed lines). Independent relaxation of each dot is indicated by the rainbow arrow, surface-mediated heat flow by the black arrow; the blue double-headed arrow shows an ~25-ps delay of heat transfer between lower and upper dot. The gray bars indicate the time range for the images in *F*. (*F*, *i–iii*) trSMA-STM images. The dashed blue circle indicates the patch of gold surface between the dots that is most strongly perturbed by energy flow in *ii* and *iii*. STM scanning conditions: 1.2 V, 50 pA. Laser power density for all images: 1.3–3 W/mm^2 (pump, 400 nm), 1.5 W/mm^2 (probe, 800 nm). (Scale bars = 5 nm.)

simultaneously. In principle, if dots on path 2 could be purified, very high quantum yields should be possible with carbon dots because the two pathways are highly dot-specific (inhomogeneous).

Regarding the signal amplitudes S_c, S_s, and S_f, the more diffuse core state c blocks tunneling over a wider area of the dot than the localized surface state s, the reason why S_c is on average larger than S_s or S_f in Table 1 and *SI Appendix*, Fig. S1. Along the same lines, when $S_f > S_s$ in some of the transients a secondary increase of signal is observed, which can be fitted quantitatively with our model (e.g., *SI Appendix*, Figs. S8, S9, and S12).

Single-particle pump–probe data from trSMA-STM provides access to the individual mechanism of excited-state migration for each carbon dot but can also be compared with bulk results. A global fit to the two classes of dots using the kinetic model yields an average core-surface migration in 0.4 ps, a slower relaxation to the ground state averaging 19 ps for dots following path 1, and relaxation to the long-lived surface state f averaging 2 ps for dots on path 2 (Fig. 5 and *SI Appendix*). Thus, the three relaxation times measured by bulk experiments (Table 1) are entirely plausible. To check consistency with bulk data further, we interpolated time points to average the single-particle traces together. By applying a conventional triple-exponential fit to the ensemble average of 12 single-dot traces in Fig. 5, we obtained fast (1.7 ± 0.2 ps), medium (5.1 ± 0.9 ps), and slow (39 ± 6 ps) time constants, in good agreement with bulk results in Table 1 (19, 20). (*SI Appendix*, Table S1 has results for all carbon dots.) The 1.7 ps fast phase is likely an overestimate of the 0.4 ps phase we obtain for individual dots and that also has been measured in the bulk, due to misregistration of "time zero" when the individual traces are averaged.

Phonon–Electron Coupling Explains Dot-Surface Energy Flow. The observations in Fig. 4 (21–23) suggest a simple model for energy flow from carbon dots to the surface or nearby dots. In the first

Table 1. Single-dot lifetimes and comparison with fluorescence up-conversion measurements (bulk) for carbon dots in Fig. 3, and ensemble fits

Three sample traces (see also *SI Appendix*)	τ_{cs}, ps	τ_{sf}, ps	τ_{sg}, ps	τ_{fg}, ns	S_s: S_f: S_c
Trace 1	0.4	17.3	*	2.6 ± 0.1†	0.52:0.26:1
Trace 2	0.4	0.7	*	2.6 ± 0.1	1:0.43:1
Trace 3	0.4	*	0.3	2.6 ± 0.1	0.3:–:1
Global fit (kinetic model)	0.4	2 ± 0.3	19 ± 2	2.6 ± 0.1	0.88:0.7:1
	τ_1, ps	τ_2, ps	τ_3, ps	τ_4, ns	
Triple-exponential fit of averaged data	1.7 ± 0.2	5.1 ± 0.9	39 ± 6	2.6 ± 0.1	
Bulk solution (450-nm excitation) (25)	0.4 ± 0.1	2.4 ± 0.2	39 ± 2	1.2 ± 0.2	

A table for all 12 dots measured can be found in *SI Appendix*.
*Too slow to be fitted.
†Lower limit from our TRPL measurement (2.6 ± 0.1 ns at 393-nm excitation, *SI Appendix*, Fig. S17).

example, following fast independent relaxation within the dots, optical phonons from both dots couple with conduction electrons on the gold surface, particularly in the valley between dots, to dissipate heat. The excited electrons spread out in the valley first due to scattering at the grain boundary (21). At long times, carriers finally are excited across the surface, leading to a depressed tunneling current.

In the second example, the fast relaxation step also occurs independently for each dot. The optical phonon–electron coupling step occurs faster for the lower dot (Fig. 4 *F*, ii), eventually heating the upper dot with an ∼25-ps delay, changing its transient absorption. From the 25-ps timescale and 6-nm separation, we calculated the effective thermal conductivity of our gold film to be ∼50 W m^{-1}·K^{-1} (*SI Appendix*), 30% lower than the reported literature on the heat conductivity of 7-nm gold films (62 W m^{-1}·K^{-1}) (23). The lower effective conductivity could be due to a dot–gold conduction bottleneck in this heat transfer process.

In summary, trSMA-STM is able to observe the flow of excitation within single carbon dots, as well as nanoscale heat flow from dots to the surface and to other dots with single-nanometer resolution on a subpicosecond timescale. The initial fast process of core-to-surface relaxation is similar for all dots we observed, but after that they fall into two classes: those that rapidly relax back to the ground state, and those that remain in a long-lived surface state, ready to fluoresce. Based on this clean divide in behavior, it should be possible in principle to prepare or purify an ensemble of dots with very high quantum yield because the moderate bulk quantum yield is not intrinsic to individual dots. Further relaxation of dot energy into the environment can be explained by coupling to electrons in the conductive gold substrate via optical phonon–conduction electron coupling. The quantitative result indicates that heat conductivity is slightly lower than in the bulk, indicating a bottleneck at the dot–surface contact. Finally, we observe some dynamics when the order of pulses is reversed ($t < 0$), which is likely due to midgap states' absorption, and will be interesting to investigate in more detail in the future.

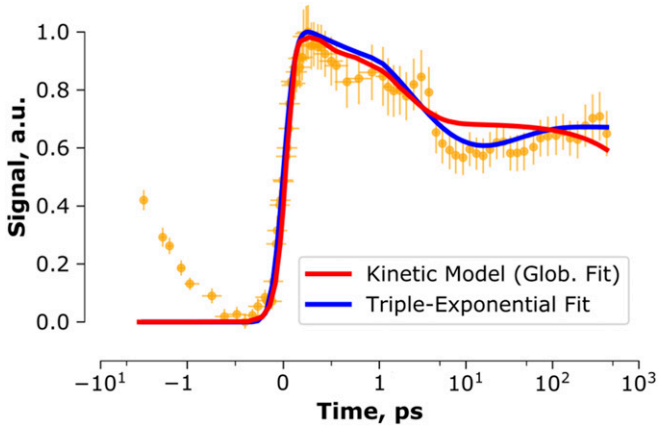

Fig. 5. Kinetic model ensemble data fit. Kinetic model global fit of the long-lived pathways and the rapidly relaxing pathways averaged in a 9:3 ratio (red) and a global fitting of the same overall data set (blue). The minor tick marks on the x axis correspond to divisions at 0.5, which are on a linear scale between −1 and 1 ps and on a log scale outside that range. The horizontal and vertical bars are the SD of the mean of data points from different individual particles averaged together as discussed in the text. The increase of experimental signal at $t < 0$ is due to absorption by gap states at 800 nm, as characterized by absorption spectra and I-V curve measurements in ref. 7.

Methods

Sample Preparation and Characterization. Dots were made by solvothermal synthesis from 1,2,4,5-benzenetetra-carboxylic acid and 2,7-diaminofluorene and characterized as in ref. 7. We selected blue dots with strong absorption at 400 nm and relatively weak absorption at 800 nm for our experiments. Their fluorescence maximum is at 475 nm as shown in ref. 7. Bulk fluorescence lifetime was measured for carbon dots at an excitation wavelength of 390 nm with an emission range of 400–700 nm (*SI Appendix*, Fig. S17). A solution of 1 μg/mL of carbon dots in ethanol is prepared and tested for fluorescence by exposing to the 400-nm laser prior to deposition. The purified carbon-dot solution is deposited on a pristine PtAu substrate fabricated according to previously reported procedure (24) by aerosol deposition using nitrogen as the carrier gas.

trSMA-STM. See *SI Appendix, Methods* for full details. As in conventional pump–probe transient absorption spectroscopy, two ultrafast pulses (400 and 800 nm derived from a Ti:sapphire oscillator with 80-MHz repetition rate, 100-fs full width at half maximum) interact with the sample through the back of the transparent gold substrate. A few milliwatts of laser power is collimated to ∼0.1-mm diameter and need not be focused because of tip enhancement and because the tip determines spatial resolution, not the diffraction limit of the excitation light (14). Time 0 is determined by cross-correlation using a beta barium borate (BBO) crystal, and pulses are aligned via a flip-in mirror through a pinhole outside the ultra-high vacuum (UHV) STM chamber located at the same distance from the collimating lens as the sample.

Each pulse train (400 and 800 nm) is separately modulated by a chopper wheel (Fig. 1) at different frequencies near the mechanical bandwidth of the STM, but well below the electronic bandwidth of the tunneling current amplifiers. Thus, the STM mechanical response to laser modulation is reduced, leading to oscillations in the tunneling current as laser-excited electrons in the carbon-dot block tunneling (after the pump beam) or are further excited to enable tunneling again (after the probe beam). Tunneling current modulation is detected by a lock-in amplifier. The lock-in frequency is set to the sum frequency of the two choppers (whose frequencies are roughly in the Golden Ratio ∼1.61) so only a transient absorption signal due to both laser beams is detected.

The sum-frequency reference for the lock-in amplifier was generated by detecting each laser with a fast photodiode and combining the modulated signals in an AD633 frequency mixer (Analog Devices) followed by band-pass filtering to remove the fundamental and overtone frequencies of the two independently modulated lasers. Additional details are described in *SI Appendix*.

CHEMISTRY

Data Availability. All study data are included in the article and/or *SI Appendix*.

ACKNOWLEDGMENTS. This work was funded by the James R. Eiszner Chair in Chemistry and a Fellowship to H.A.N from the Department of Chemistry at the University of Illinois at Urbana-Champaign. D.P. acknowledges funding from National Institute of Biomedical Imaging and Bioengineering grant R03EB028026-01 and National Heart, Lung, and Blood Institute grant R43HL151073-01A1. We acknowledge assistance from Julio Soares (Materials Research Lab, University of Illinois at Urbana-Champaign) for time-resolved photoluminescence (TRPL) measurements.

1. J. Jiang, T. Xu, J. Lu, L. Sun, Z. Ni, Defect engineering in 2D materials: Precise manipulation and improved functionalities. *Research (Wash D C)* **2019**, 4641739 (2019).
2. X. Zhang *et al*., Poly(4-styrenesulfonate)-induced sulfur vacancy self-healing strategy for monolayer MoS_2 homojunction photodiode. *Nat. Commun.* **8**, 15881 (2017).
3. N. Tsumori *et al*., Quasi-MOF: Exposing inorganic nodes to guest metal nanoparticles for drastically enhanced catalytic activity. *Chem* **4**, 845–856 (2018).
4. M. Behrens *et al*., The active site of methanol synthesis over Cu/ZnO/Al2O3 industrial catalysts. *Science* **336**, 893–897 (2012).
5. M. Lunz, A. L. Bradley, W.-Y. Chen, Y. K. Gun'ko, Förster resonant energy transfer in quantum dot layers. *Superlattices Microstruct.* **47**, 98–102 (2010).
6. H. Ding, S.-B. Yu, J.-S. Wei, H.-M. Xiong, Full-color light-emitting carbon dots with a surface-state-controlled luminescence mechanism. *ACS Nano* **10**, 484–491 (2016).
7. H. A. Nguyen, I. Srivastava, D. Pan, M. Gruebele, Unraveling the fluorescence mechanism of carbon dots with *sub*-single-particle resolution. *ACS Nano* **14**, 6127–6137 (2020).
8. D. Nguyen *et al*., Orientation-dependent imaging of electronically excited quantum dots. *J. Chem. Phys.* **148**, 064701 (2018).
9. J. Miao, P. Ercius, S. J. L. Billinge, Atomic electron tomography: 3D structures without crystals. *Science* **353**, aaf2157 (2016).
10. H. Offenbacher *et al*., Orbital tomography: Molecular band maps, momentum maps and the imaging of real space orbitals of adsorbed molecules. *J. Electron Spectrosc. Relat. Phenom.* **204**, 92–101 (2015).
11. M. Semeniuk *et al*., Future perspectives and review on organic carbon dots in electronic applications. *ACS Nano* **13**, 6224–6255 (2019).
12. I. Srivastava *et al*., Surface chemistry of carbon nanoparticles functionally select their uptake in various stages of cancer cells. *Nano Res.* **10**, 3269–3284 (2017).
13. S. K. Misra *et al*., Macromolecularly "caged" carbon nanoparticles for intracellular trafficking via switchable photoluminescence. *J. Am. Chem. Soc.* **139**, 1746–1749 (2017).
14. E. S. Carmichael, J. B. Ballard, J. W. Lyding, M. Gruebele, Frequency-modulated, single-molecule absorption detected by scanning tunneling microscopy. *J. Phys. Chem. C* **111**, 3314–3321 (2007).
15. S. Wang *et al*., Photoinduced carrier generation and distribution in solution-deposited titanyl phthalocyanine monolayers. *Chem. Mater.* **31**, 10109–10116 (2019).
16. D. Nguyen *et al*., Imaging of carbon nanotube electronic states polarized by the field of an excited quantum dot. *ACS Nano* **13**, 1012–1018 (2019).
17. C. M. Carbonaro *et al*., On the emission properties of carbon dots: Reviewing data and discussing models. *J. Carbon Res.* **5**, 60 (2019).
18. P. Kumar, H. B. Bohidar, Universal correlation between solvent polarity, fluorescence lifetime and macroscopic viscosity of alcohol solutions. *J. Fluoresc.* **22**, 865–870 (2012).
19. S. Khan, A. Gupta, N. C. Verma, C. K. Nandi, Time-resolved emission reveals ensemble of emissive states as the origin of multicolor fluorescence in carbon dots. *Nano Lett.* **15**, 8300–8305 (2015).
20. N. Basu, D. Mandal, Time-resolved photoluminescence of pH-sensitive carbon dots. *Carbon* **144**, 500–508 (2019).
21. T. Luo, G. Chen, Nanoscale heat transfer–From computation to experiment. *Phys. Chem. Chem. Phys.* **15**, 3389–3412 (2013).
22. S. Shen, A. Mavrokefalos, P. Sambegoro, G. Chen, Nanoscale thermal radiation between two gold surfaces. *Appl. Phys. Lett.* **100**, 233114 (2012).
23. H. Lin, S. Xu, C. Li, H. Dong, X. Wang, Thermal and electrical conduction in 6.4 nm thin gold films. *Nanoscale* **5**, 4652–4656 (2013).
24. L. Nienhaus *et al*., Transparent metal films for detection of single-molecule optical absorption by scanning tunneling microscopy. *J. Phys. Chem. C* **118**, 13196–13202 (2014).
25. X. Wen, P. Yu, Y.-R. Toh, X. Hao, J. Tang, Intrinsic and extrinsic fluorescence in carbon nanodots: Ultrafast time-resolved fluorescence and carrier dynamics. *Adv. Opt. Mater.* **1**, 173–178 (2013).